

AD \_\_\_\_\_

Award Number:  
W81XWH-10-1-0519

TITLE:  
Massively Parallel Rogue Cell Detection Using Serial Time-  
Encoded Amplified Microscopy of Inertially Ordered Cells in High-  
Throughput Flow

PRINCIPAL INVESTIGATOR:  
Dino Di Carlo, Bahram Jalali

CONTRACTING ORGANIZATION:  
  
University of California, Los Angeles  
Los Angeles, CA 90095

REPORT DATE:  
August 2012

TYPE OF REPORT:  
Final

PREPARED FOR: U.S. Army Medical Research and Materiel Command  
Fort Detrick, Maryland 21702-5012

DISTRIBUTION STATEMENT:

x Approved for public release; distribution unlimited

The views, opinions and/or findings contained in this report are those of the author(s) and should not be construed as an official Department of the Army position, policy or decision unless so designated by other documentation.

REPORT DOCUMENTATION PAGE				Form Approved OMB No. 0704-0188	
Public reporting burden for this collection of information is estimated to average 1 hour per response, including the time for reviewing instructions, searching existing data sources, gathering and maintaining the data needed, and completing and reviewing this collection of information. Send comments regarding this burden estimate or any other aspect of this collection of information, including suggestions for reducing this burden to Department of Defense, Washington Headquarters Services, Directorate for Information Operations and Reports (0704-0188), 1215 Jefferson Davis Highway, Suite 1204, Arlington, VA 22202-4302. Respondents should be aware that notwithstanding any other provision of law, no person shall be subject to any penalty for failing to comply with a collection of information if it does not display a currently valid OMB control number. <b>PLEASE DO NOT RETURN YOUR FORM TO THE ABOVE ADDRESS.</b>					
1. REPORT DATE) 01-Aug-2012		2. REPORT TYPE Final		3. DATES COVERED 01 Aug 2010 - 31 Jul 2012	
4. TITLE AND SUBTITLE Massively Parallel Rogue Cell Detection Using Serial Time-Encoded Amplified Microscopy of Inertially Ordered Cells in High-Throughput Flow				5a. CONTRACT NUMBER	
				5b. GRANT NUMBER W81XWH-10-1-0519	
				5c. PROGRAM ELEMENT NUMBER	
6. AUTHOR(S) Dino Di Carlo, Bahram Jalali  dicarlo@seas.ucla.edu				5d. PROJECT NUMBER	
				5e. TASK NUMBER	
				5f. WORK UNIT NUMBER	
7. PERFORMING ORGANIZATION NAME(S) AND ADDRESS(ES) University of California, Los Angeles Los Angeles, CA 90095-1600				8. PERFORMING ORGANIZATION REPORT NUMBER	
9. SPONSORING / MONITORING AGENCY NAME(S) AND ADDRESS(ES) U.S. Army Medical Research And Materiel Command Fort Detrick, Maryland 21702-5012				10. SPONSOR/MONITOR'S ACRONYM(S)	
				11. SPONSOR/MONITOR'S REPORT NUMBER(S)	
12. DISTRIBUTION / AVAILABILITY STATEMENT  Approved for public release; distribution unlimited					
13. SUPPLEMENTARY NOTES					
14. ABSTRACT We developed a high-throughput imaging cytometry system for high accuracy identification of rare circulating breast cancer cells in blood. Key accomplishments include: 1. Construction of a serial time encoded amplified microscopic camera, Nomarski system, and laser scanner for blur free imaging of breast cancer cells and blood cells in flow with and without microparticle labels to EpCAM on the cell surfaces. 2. Development of microfluidic devices compatible with the optical system in rigid optically transparent materials. 3. Development of a real-time field programmable gate array image analyzer for high-throughput image-based screening, and 4. Inline sample preparation microfluidic system for inline microparticle labeling of breast cancer cells without lossy centrifugation steps. The work has yielded high accuracy ~ 75% identification of spiked breast cancer cells from blood with a false positive rate of 1 MCF7 breast cancer cell in 1,000,000 white blood cells, a few orders of magnitude better accuracy than flow cytometry scatter and fluorescence measurements alone.					
15. SUBJECT TERMS Microfluidics, circulating tumor cells, rare cell detection, high-speed imaging, flow cytometry					
16. SECURITY CLASSIFICATION OF:			17. LIMITATION OF ABSTRACT  UU	18. NUMBER OF PAGES  22	19a. NAME OF RESPONSIBLE PERSON USAMRMC
a. REPORT U	b. ABSTRACT U	c. THIS PAGE U			19b. TELEPHONE NUMBER (include area code)

## Table of Contents

	<u>Page</u>
Introduction.....	4
Body.....	4
Key Research Accomplishments.....	16
Reportable Outcomes.....	16
Conclusion.....	17
References.....	17
Appendices.....	17

## Introduction

We aim to develop an instrument for high-throughput identification of rare circulating breast cancer cells to enable early detection and analysis of treatment effectiveness. To address this challenge, we have developed an automated flow-through single-cell optical microscopy system that can evaluate, diagnose, and screen a large population of cells in a short time. Innovations have been made in label-free cell imaging, identification of materials, sample preparation, and hybrid dispersion laser scanning. We have further advanced our high-speed imaging modality to include Nomarski, an enhanced optical contrast modality, such that high-throughput detection and analysis of unstained cells is now possible. This method greatly enhances our ability to identify breast cancer cells in blood and builds upon a unique integration of (i) an ultrafast optical imaging modality known as Nomarski serial time-encoded amplified microscopy (N-STEAM) for blur-free and high-contrast imaging by differential interference contrast (DIC) of label-free cells in high-speed flow using a Nomarski prism, (ii) inertial microfluidic technology for sheath-free focusing and ordering of cells with inertial forces, and (iii) hybrid optoelectronic image processing circuitry for real-time image processing. The integrated system combines the high-contrast capability of DIC with the STEAM system we have developed, where microfluidic flow is transformed into a series of “E-slides” – an electronic version of glass slides – on which cells of interest are digitally analyzed. This property enables fully automated real-time image-recording and classification of a large number of cells through their morphological and biochemical features, with increased contrast and no staining required. The most appropriate materials for the flow cell for such a system were assessed, and thermoset polyester (TPE) was confirmed as the most appropriate for its hardness, optical transparency in wavelengths of interest, and inertial focusing capability. To improve the system and enable labeling with contrast enhancing beads without additional steps, a purely hydrodynamic strategy for sample preparation of cells exchanged across multiple streamlines of solutions has been devised, known as rapid inertial solution exchange (RInSE). This method employs inertial focusing to expose cells to well-defined streamlines of solutions at rates exceeding 1000 particles per second, for applications such as cell labeling and washing – for example with microparticles for enhanced imaging without centrifugation steps. In addition, we have developed a new type of hybrid dispersion laser scanner that increases scan rates over conventional state-of-the-art scanners by several orders of magnitude. This method uses no mechanical nor active electronic components, enabling ultrafast inertia-free scans in the industrially and biomedically important spectral band (i.e.,  $\sim 800$  nm).

## Body

### N-STEAM

Our N-STEAM imaging system builds upon our serial time-encoded amplified microscopy system, STEAM, to harness

its high speed imaging capability and combine it with the high-contrast of DIC afforded by the Nomarski prism. The result is high speed imaging of label-free cells that will greatly enhance our ability to distinguish morphological changes, leading to increased breast cancer cell identification.

The N-STEAM employs a Nomarski prism (also known as modified Wollaston prism) and spatial light dispersers (e.g., a pair of diffraction gratings) to produce two 1D spatially-dispersed orthogonally-polarized beams as illustrated in Fig. 1(a). It, then, illuminates two adjacent points on the object with each wavelength component but different polarizations. The illumination beams travel through the two incident points on the transparent object and hence, they experience different phase shifts associated with the optical path lengths (i.e., the product of the refractive

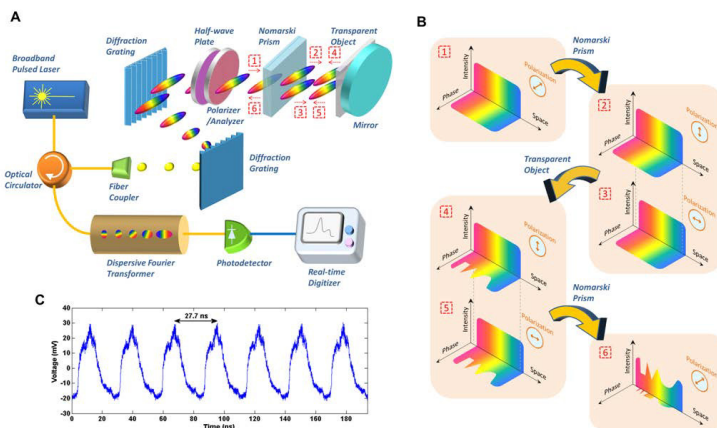


Fig. 1. Nomarski serial time-encoded amplified microscopy (N-STEAM). N-STEAM builds on a unique combination of STEAM's high-speed imaging capability and DIC/Nomarski microscopy's ability to image transparent objects without staining. (a) Schematic of the N-STEAM imager. The N-STEAM uses a Nomarski prism to encode the optical path length (the product of the refractive index and thickness) of the object into the optical spectrum of the illumination beam. (b) Evolution of the intensity, phase, and polarization of the illumination beam(s) at different points in the system. (c) Temporal waveform that shows N-STEAM's frames (line scans) at 36.1 MHz, corresponding to a repetition period of 27.7 ns.

index and thickness) of the two incident points on the object [Fig. 1(b)]. By recombining the two phase-encoded beams using the same Nomarski prism, the differential phase information is converted into an intensity modulation. In other words, the optical path length difference between the two incident points results in constructive / deconstructive interference for each wavelength. The image-encoded spectrum [Fig. 1(b)] is then converted into a temporal data stream, stretched in time, and simultaneously amplified using an amplified dispersive Fourier transformation. The time stretch allows the image to be digitized by a conventional electronic digitizer. Also, the optical image amplification ( $\sim 20$  dB) over a wide optical bandwidth (as large as 60 nm) overcomes the loss of signal at high frame rates and is a key feature of this method. The temporal waveform in Fig. 1(c) indicates the repetitive pulses (corresponding to the line scans) detected by a single-pixel photodetector and illustrates the operation of N-STEAM at 36.1 MHz frame rate. In other words, N-STEAM's real-time capture of time-domain pulses enables pulse-to-pulse (frame-by-frame) image acquisition at 36.1 MHz rate.

A phase contrast implementation of the STEAM imager based on Hilbert transform has been reported by us before. In that implementation, which does not use the Nomarski technique, the time domain signal is upconverted to a higher modulation frequency; therefore, the requirements on the speed of the digitizer is more demanding, and digital signal processing is required to perform the Hilbert transform. The present Nomarski based technique does not have such requirements.

In an implementation of N-STEAM, the broadband pulse laser is a mode-locked laser with a center wavelength of 1560 nm and a pulse repetition rate of 36.1 MHz. A highly nonlinear fiber and optical band-pass filter following the laser produces a train of pulses with  $\sim 20$  nm bandwidth centered at 1591 nm as an illumination beam. Using a pair of diffraction gratings with 1100 lines/mm groove density, the pulses are spatially-dispersed into a 1D rainbow pattern enabling 1D line-scanning of the object. The 1D spatially-dispersed beam (i.e., 1D rainbow) is sent to a half-wave plate and a polarizer to rotate the polarization state of the light and ensure 45-degree linear polarization incident on the Nomarski prism. The Nomarski prism splits the illumination beam into two orthogonally-polarized 1D rainbow patterns (0 and 90 degrees).

The design of the Nomarski prism and the subsequent optics are such that the two orthogonally-polarized beams are incident on the object in the direction normal to the direction of the line scan. A mirror is placed at the back of the object to return the phase-encoded beams to the same optics, which results in double passing of the illumination beams through the object, and hence, doubles the phase shifts. After recombining the phase-encoded beams using the same Nomarski prism, the spectrally-encoded beam is directed to a spool of optically-pumped dispersive fiber (with dispersion value of  $-1373$  ps/nm) via an optical circulator to perform amplified dispersive Fourier transformation (gain of  $\sim 20$  dB). The time-encoded optical pulses are then captured by a high-speed photodetector with 10 GHz bandwidth and digitized by a real-time digitizer with 16 GHz bandwidth and 50 GS/s sampling rate (Tektronix – DPO71604). Digital signal processing including background and noise removal is performed offline to reconstruct the image of the object under test.

To demonstrate our method, we performed imaging of a transparent structure using N-STEAM. The object is

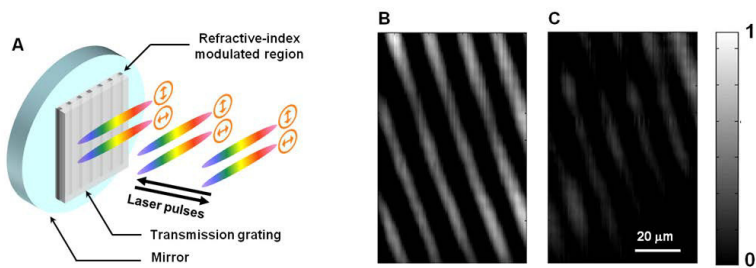


Fig. 2. (a) Schematic of the transparent refractive-index modulated structure aligned with the illumination beams. Images of a transparent refractive-index modulated structure captured using N-STEAM with (b) and without (c) the Nomarski prism. The imager without the prism is equivalent to STEAM, while the enhancement in the image contrast was obtained with the Nomarski prism (i.e., N-STEAM). The second dimension of the images was obtained by translating the sample in the direction normal to the line scans. The comparison of the images indicates significant contrast enhancement obtained by the N-STEAM.

a transparent material with a periodic refractive-index modulation [i.e., a transmission grating with a groove density of 70 lines per millimeter, Fig. 2(a)]. Figures 2(b) and 2(c) compare the reconstructed two-dimensional (2D) images with N-STEAM and STEAM, respectively. The second dimension of the images was obtained by translating the

images in the direction orthogonal to that of the line scans. The design of the object is such that the refractive-index modulation is small; hence, the reflection from different points on the object is below the sensitivity of the STEAM imager. With the Nomarski prism, the system provides

differential phase-contrast in imaging of the object [Fig. 2(b)]. The captured image without the Nomarski prism (i.e., using STEAM without DIC implementation) shows the normalized reflectivity map of the object [Fig. 2(c)]. As evident from the images, significant contrast-enhancement is achieved by using N-STEAM. The high-intensity lines in the image are  $\sim 14 \mu\text{m}$  apart, which agrees with the specifications of the transparent structure.

To demonstrate the use of our method in high-speed high-contrast imaging of unstained biological cells for identification of breast cancer cells in blood, we also performed imaging of fast-flowing unstained white blood cells in a microfluidic channel. White blood cells were isolated from whole blood by hypotonic lysis of red blood cells and resuspended in phosphate buffered saline. To acquire 2D images of the cells, they flow [Fig. 3(a)] at a flow speed of 1

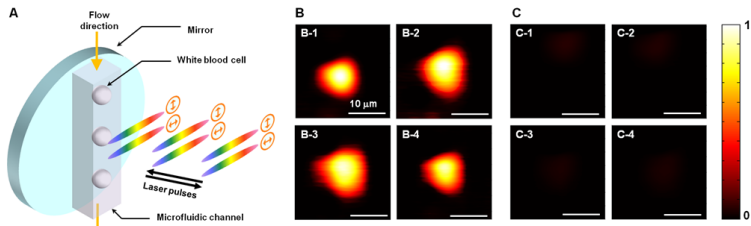


Fig. 3. (a) Schematic of the microfluidic channel aligned with respect to 1-D rainbow illumination pulses. Images of unstained white blood cells captured by N-STEAM, (b) with and, (c) without the Nomarski prism. The flow rate was 1 meter/s. The image contrasts obtained by N-STEAM is  $>15$  times larger than those of obtained by STEAM. The rest of scale bars,  $10 \mu\text{m}$ .

meter/s in the direction orthogonal to that of the line scans – providing 400-500 image pixels in the flow direction for each white blood cell. Figures 3(b) and 3(c) compare the images of white blood cells captured by N-STEAM and STEAM, respectively. The image captured by N-STEAM [Fig. 3(b)] is based on the relative phase shift between the illumination beams when propagating through the cell, while the image captured by STEAM [Fig. 3(c)] shows the reflection from the surface of the cell. Note that the color coding in Fig. 3(b) represents the normalized optical path length of the cell, while

that in Fig. 3(c) represents the normalized reflectivity of the cell. Interestingly, the image contrasts of the white blood cells captured by N-STEAM is  $>15$  times higher than those of captured by STEAM; that is equivalent to  $\sim 12$ -dB signal-to-noise ratio (SNR) improvement over STEAM. This is due to poor refractive-index contrast and/or absorption of unstained white blood cells compared to their aqueous surrounding (i.e., phosphate buffered saline). Since N-STEAM reveals the optical path length of the cell (i.e., the product of refractive index and size), it can be potentially used to distinguish different types of cells that are similar in size, and hence suggests an improved path to high-throughput imaging-based cell analysis beyond traditional STEAM.

For STEAM alone, our statistical analysis of the capture efficiency indicates that the field-programmable digital image processor can identify extremely rare cells with a high efficiency of 75% (limited by the imperfect coating efficiency and missing smaller MCF7 cells in the FPGA selection process). Furthermore, our receiver operating characteristic (ROC) curve analysis of the results indicates that our method is sufficiently sensitive for detection of  $\sim 1$  MCF7 cell in a million white blood cells and is 100 times better in terms of false positive rate than the conventional flow cytometer with either fluorescence or scatter measurements (Figure 4), yet without sacrificing throughput. Here all the measurements were performed at a throughput of 100,000 cells/s, corresponding to screening of 10 mL of lysed blood in less than 15 minutes. Further improvements can be expected when implementing N-STEAM.

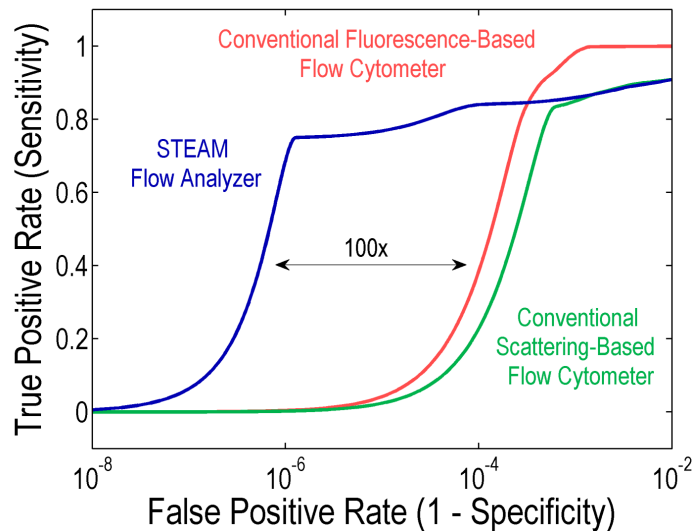


Fig. 4 ROC curve analysis of the STEAM flow analyzer in comparison with the conventional flow cytometer for both fluorescence and scattering measurements. Our method is sufficiently sensitive for detection of  $\sim 1$  MCF7 cell in a million white blood cells (i.e., a false positive rate of  $\sim 10^{-6}$ ) and is two orders of magnitude better in terms of false positive rate than the conventional flow cytometer yet without sacrificing throughput.

We have demonstrated a method that enables high-speed contrast-enhanced image acquisition of transparent objects without the need for chemical staining. This imaging modality, N-STEAM, fills the contrast and speed gap between phase imaging-based techniques and STEAM imager. It couples the high-speed capability of the STEAM imager and differential phase contrast imaging of DIC / Nomarski microscopy. As the proof of concept, we performed imaging of a transparent structure and white blood cells in flow at 33 ps shutter speed and 36.1 MHz frame rate. N-STEAM holds promise for high-throughput imaging of unstained biological cells with improved performance over 1<sup>st</sup> generation STEAM.

## Materials for Microfluidic Devices

We conducted a study to identify the optimal materials for prototyping of microfluidic devices compatible with the STEAM flow system and suitable for rapid detection of circulating breast cancer cells from blood. A microfluidic prototyping material for a research laboratory environment should be easy to use. This includes having a short time to produce a chip, low technical difficulty, high repeatability, and high success rate. The success of PDMS as a prototyping material in the microfluidics community is due to it satisfying these criteria. Here we discuss these parameters for a range of prototyping materials beyond PDMS. The time required for PDMS device production as indicated in Fig. 5 is roughly 3 h (1 h + 2 h of curing) once the silicon master is fabricated. Bonding for sealing of channels can be established between PDMS and PDMS, or other materials like glass or silicon. However, for many labs, PDMS bonding has variable success, depending on humidity and temperature, plasma equipment and power, ratio of crosslinking agent/polymer, and also last but not least, operator skill. For example, for 10 PDMS chips, our success rate for chip sealing varies from 50 to 100% depending on the operator. Fabrication using TPE, as described in Fig. 5, is also easy and quick (1 h) once the mold is generated, but a final curing step at room temperature requires 1 day. Contrary to PDMS, sealing of TPE to glass slides is highly reproducible, with high yield independent on the operator skill or environmental conditions. As an indication, our success rate for chip fabrication and sealing was 90%. On 10 TPE chips, we obtained 9 homogenous and strong bonds, the failed bond being due to operator error and presence of air bubbles in the TPE mix. Moreover, TPE chips were also successfully sealed to other substrates like dielectric and metallic mirrors used for the STEAM system while PDMS does not form a permanent bond to these substrates. A drawback of TPE fabrication is the necessity of precisely weighing and mixing several components under a fume hood, due to the noxious fumes from the resin. On the contrary, PUMA does not require handling under special ventilation. No mixing of components is required as the resin is directly poured on the mold and crosslinked under UV light. The fabrication is simple and a chip can be fabricated in a similar time as PDMS chips - 3 h (1 h + 2 h of cooling). The success rate for bonding is around 90% (for 10 chips and 3 devices/chip), with the failure mode being that the channels closer to the chip edges may not be well-sealed. Using a homemade suction system reduces bending of the polymer during demolding and improves homogeneity in bonding. Similarly to PUMA, prototyping with NOA does not require special manipulation precautions or mixing of components as the resin is directly poured into the mold. Bartolo et al present a method in which a thin NOA chip is sandwiched between two glass slides. The addition of this second glass slide, used to handle the thin NOA layer without bending, requires a drilling step, which complicates the fabrication process. A thicker NOA chip can be easily manipulated without this second glass slide. However, the fabrication of thicker devices is made challenging by the fast crosslinking time of the resin (only 1 or 2 s with our UV lamp) and thus requires fine tuning of the exposure dose to match with the thickness of the chip. Indeed, NOA in the center of a thick chip must be cured for correct demolding but a superficial uncured layer should still be present to allow subsequent sealing to a cover. We obtained 80% (for 10 chips and 3 devices/chip) as a success rate for chip fabrication and sealing, the main issue being the presence of residual uncured resin inside the channels leading to non-uniform thickness.

		PDMS	TPE	PUMA	NOA
Material Properties	Hardness	-	++	+	+
	Biocompatibility	+	-	++	++
	Optical Transparency	++	+	+	+
	Solvent Compatibility	-	+	+	+

Performance for Fast Prototyping And High Pressure Injections	Ease of Use	+	-	++	++
	Fabrication Time	1h + 2h	1h + 1 day	1h + 2h	1h + 2h
	Cost	<\$1/mL	~\$4.5/mL	~\$2.2/mL	<\$1/mL
	Replication Fidelity	+	+	+	+
	Channel Deformation	-	++	+	+
	Stabilization Time	-	++	++	++
	Maximum Pressure	-	++	+	+
	Inertial Focusing	-	++	+	+

Table 1 Overall performance of PDMS, TPE, PUMA and NOA as materials for rapid prototyping of microfluidic devices and high pressure injections

As summarized in Table 1, rapid prototyping in PDMS is advantageous because of its low cost, quick and straightforward fabrication, and its biocompatibility which allows its use for many applications. Nevertheless, its elastomeric nature and low elastic modulus result in many drawbacks. Indeed, even at low flow rates significant channel deformation occurs as the channel inlet pressure increases. This distortion introduces a non-linearity into the pressure flow relationship and the associated stabilization time can reach some minutes, even some hours for viscous fluids. Further, the sealing to glass substrates fails at around 30–50 PSI, making PDMS devices inappropriate for high pressure injections. Fabrication in TPE is more complex but still accessible, quick and cheap. TPE bonding was found to be highly reproducible and stronger than PDMS. The high rigidity of TPE, similar to glass, is also of great interest and proved ideal for high pressure injections needed in our high-throughput cytometry system. TPE compliance is negligible and fluidic resistance is not dependent on the pressure, thus resulting in a linear relationship between pressure drop and flow and a fast stabilization time, and low morphing of channels in response to flow which allows for an easier aligned optical system. The suitability of PUMA and NOA for high pressures lies between PDMS and TPE as the sealing strength is weaker than for TPE but still higher than PDMS, and channel deformation is still visible with PUMA when pressures increase. All polymers tested (TPE, PUMA and NOA) (i) show good transmission in the visible light region but similarly block UV light, (ii) can be replicated over a wide range of feature sizes, and (iii) possess a solvent resistance better than PDMS. For these reasons, TPE was chosen as the material of choice in our integrated STEAM system.

### Rapid Inertial Solution Exchange for Inline Sample Preparation of Cancer Cells

Since our STEAM system made use of breast cancer cells in lysed blood labeled with microparticles and these steps was performed using manual centrifugation and wash steps, we conducted a study to attempt to conduct these steps on chip. That is, we performed washing of MCF7 cells from red blood cell lysis debris and after labeling with microparticles using inertial lift forces all in a passive continuous system that could be compatible with STEAM. An optimal approach should be high-throughput and offer additional functionality such as fast, uniform exchange of particles between solutions for measurement of dynamic events, precise cell/particle positioning for optical analysis, and simple manufacturability to create parallel systems for processing large samples. To these ends, we introduced a general strategy to manipulate particles to passively cross streams at high rates. The approach takes advantage of modifications in inertial focusing equilibrium position as channels merge and change aspect ratio. We establish a co-flow of a suspension and a transfer solution in such a way that particles migrate across fluid streamlines to lie within the transfer solution downstream. In particular, we engineer systems in which wall effect lift directed along the axis of particle rotation leads to particle migration across laminar streams without significant disruption of the interface. Uniquely, the rapid inertial solution exchange (RInSE) approach is purely hydrodynamic without external force fields or mechanical interactions between particles and surfaces. This minimizes wasted reagents and power, limits clogging, and can be parallelized with ease. Lateral migration across streamlines and complete solution exchange occurs within milliseconds enabling dynamic measurements and allowing short microchannels with small footprints and lower pressures. Lastly, inertial focusing serves the dual purpose of being the mechanism for exchange as well as focusing cells downstream (in position and velocity) for inline STEAM cytometric analysis.

RInSE was developed employing multiple design rules for inertial focusing which we have reported in previous work. Briefly, inertial focusing is a method for precise control of cell position in flow by controlling geometry dependent lift forces and, optionally, secondary flows present infinite-inertia confined flows. A particular design that employs these operating principles is depicted in Figure 5. Cells and particles are injected through asymmetric curving channels at a flow velocity sufficiently high to achieve precise focusing. Simultaneously, a transfer solution is pumped through a straight channel at a volumetric flow rate 1.5 to 2 times higher than the rate in the particle channel. Both inlets are immediately followed by size exclusion filters which remove large debris and aggregates. Importantly, the channels join at an angle ( $30^\circ$ ) which is low enough to avoid secondary flow-induced mixing or disturbance of the interface between the solutions. Once the channels join, the co-flowing fluid streams enter a wide, straight rectangular transfer channel. Due to the mismatch in volumetric flow rates of the two inlet channels, the transfer solution fills more than half of the transfer channel. Further, there is negligible diffusive mixing across the co-flow interface given that the Peclet number ( $Pe = LU / D$ , where  $L$  is the characteristic length scale—channel width,  $W$ , here—  $U$  is the average fluid

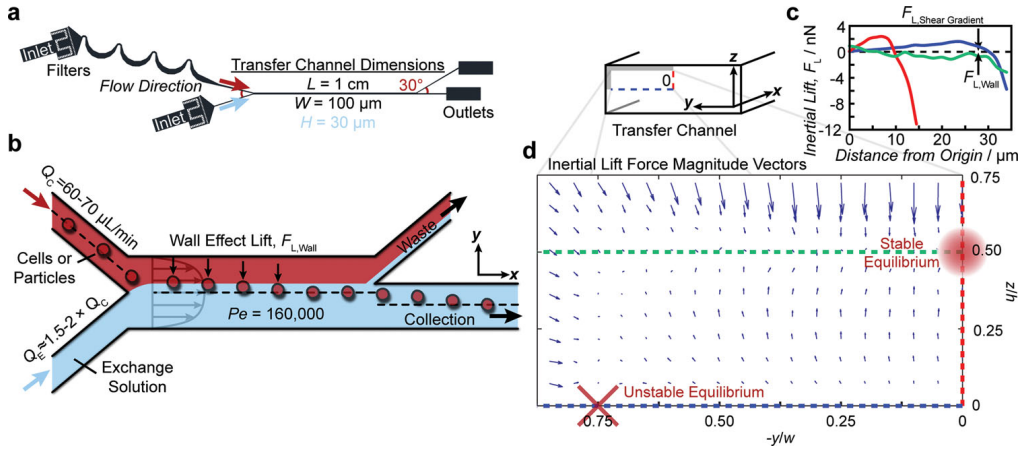


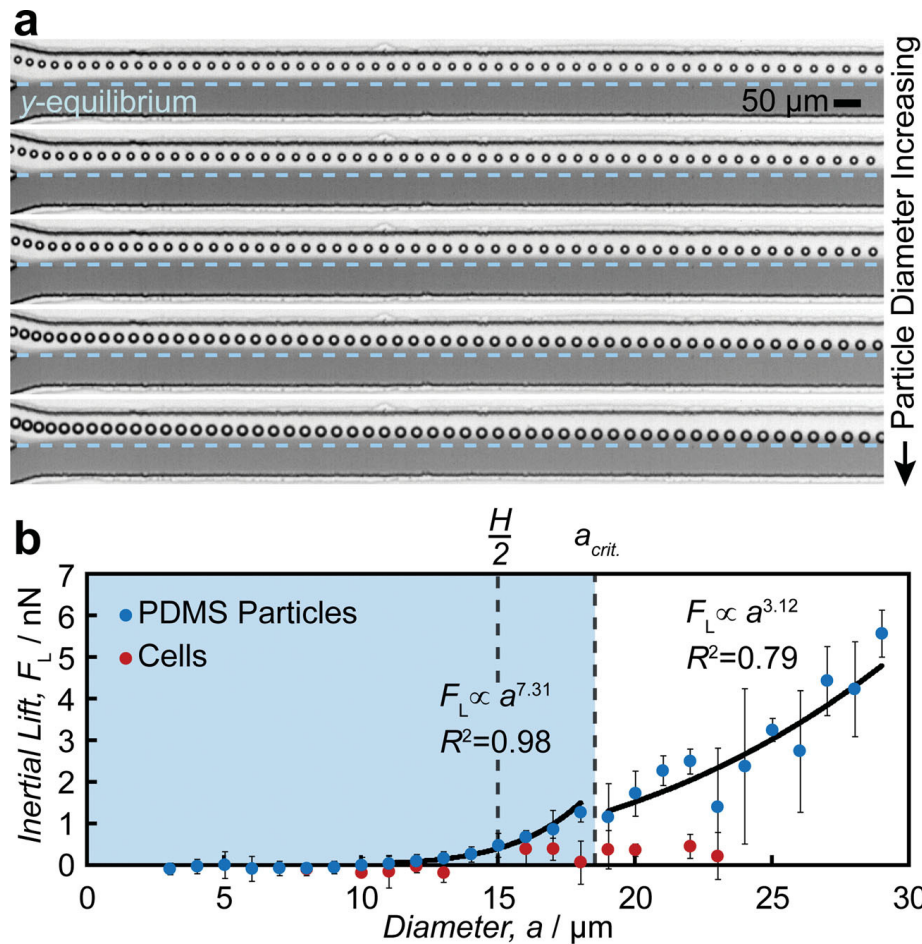
Figure 5. Design and operating principles of rapid inertial solution exchange. a) A computer-aided design of the microchannel used to fabricate the device. b) Inertial lift forces are depicted; lift-induced transfer of particles into a co-flowing solution is the mechanism of solution exchange. c) Numerically calculated lift forces acting on a  $10 \mu\text{m}$  ( $a / H = 0.25$ ) particle in a high aspect ratio microchannel ( $AR = 2:1$ ) at particle Reynolds number = 2.8. The shear gradient lift force is stronger along the short axis of high aspect ratio microchannels (red line) but is greatly diminished along the long axis (blue line) and is observed to undergo a reversal of sign when the axis is shifted to pass through the stable equilibrium (green line). d) Vector plot of numerically calculated lift forces acting on a particle at positions throughout a symmetric quadrant of a high aspect ratio microchannel ( $w = W/2$  and  $h = H/2$ ).

hydraulic diameter of the channel ( $D_h = 2WH / (W + H)$ , a function of the channel height,  $H$ , and width,  $W$ ). When oriented as depicted, these equilibrium positions are present at the center of the transfer channel (Figure 6 b) and within the transfer solution, rather than in the original suspending fluid. The resistance of the outlets is also tuned such that the resuspended particles in the transfer solution are collected in one outlet following the channel bifurcation without contamination by the original suspending fluid.

Many previous works employing inertial focusing have made use of the fact that high aspect ratio channels can have fewer equilibrium positions than square channels; however, there is currently no physical explanation for why this occurs. Due to the importance of microchannel aspect ratio for the effective operation of RInSE, it is useful to delve into this phenomenon. The aspect ratio of a rectangular channel defines the shape of the velocity field within the channel, and this velocity field in turn determines the lift forces acting on suspended particles. The magnitude of two lift forces, acting opposite one another, determine the equilibrium position of a particle: one which acts down the gradient in shear rate (Shear gradient lift:  $F_L = f_{LS} \rho U_m^2 a^3 / H$ , where  $f_{LS}$  is a lift coefficient that is proportional to product of the shear rate and the shear gradient and dependent on the local shear rate, shear gradient, and Reynolds number;  $U_m$  is the maximum fluid velocity) and one which directs particles away from walls (Wall effect lift:  $F_L = f_{LW} \rho U_m^2 a^6 / H^4$ , with a lift coefficient which does not depend strongly on the curvature of the velocity field and is

velocity, and  $D$  is the diffusivity of dissolved solutes) is over  $10^5$ , assuming diffusivities on the order of  $10^{-9} \text{ m}^2/\text{s}$ . In the transfer channel, the previously focused particles of sufficient size migrate uniformly to two equilibrium positions at the long face of the microchannel over a range of particle Reynolds numbers. The particle Reynolds Number,  $Re_P$ , is defined as  $\rho U_m a^2 / \mu D$  where  $\rho$  is the fluid density,  $U_m$  is the maximum fluid velocity,  $a$  is the particle diameter,  $\mu$  is the dynamic viscosity of the fluid, and  $D$  is the

instead proportional to the shear rate squared). The unique velocity field in a high-aspect ratio channel can explain the reduction in equilibrium positions through a modified balance of lift forces compared to square channels. In the high aspect ratio transfer channel a blunted velocity profile develops within 100  $\mu\text{m}$  of the joining of the two inlet channels. As particles are delivered to the transfer channel distal from the wall, well within the blunted region of the velocity profile with a weaker gradient in shear rate, they are expected to experience smaller shear gradient lift forces. This should lead to a dominant wall effect lift and particle migration towards the channel centerline. One should note that there are still large shear gradients in the z-axis (along the short channel dimension) which have an important role in positioning in that axis. This expected behavior is investigated using numerical simulation of the inertial lift forces acting on a 10  $\mu\text{m}$  sphere in a high aspect ratio microchannel. The lift force field is shown in one quadrant of the channel in Figure 6 d.



The inertial lift forces, employed in this strategy, are dependent on particle size and lead to a critical particle size that can be transferred for a specific geometry and flow condition. Further, by analyzing the scaling of the lift force with particle diameter we can confirm this mechanism of transfer. The lateral migration velocity of particles is experimentally determined to increase with particle size (Figure 6). An automated image analysis algorithm measured particle size and lateral migration velocity from high-speed videos. From these velocities, the lift force was calculated assuming Stokes drag ( $F_L = 3 \pi \mu a U_L$ , where  $\mu$  is the dynamic viscosity of water (0.001  $\text{kg/m} \cdot \text{s}$ );  $a$  is the particle diameter; and  $U_L$  is the lateral migration velocity of the particle). The relationship between the particle diameter and the measured lift force is depicted in Figure 6 b (blue). The scaling of  $a$  with  $F_L$  agrees with our previous numerical results for

wall effect inertial lift for rigid particles from 11 to 18  $\mu\text{m}$ ; however, beyond this critical size,  $a_{crit.}$ , which is slightly larger than half the channel height, particles span multiple flow planes and likely experience stronger shear-gradient lift that reduces the net center-directed force. Employing this lateral motion we achieve high

transfer efficiency, purity, and speeds. Of the particles ( $18.29 \pm 2.31 \mu\text{m}$ ) entering the system 97% exit through the

expected collection outlet. Additionally, the transfer solution into which particles enter was determined to be 100% pure by spectroscopy (i.e., no dilution with solution from the particle inlet).

Exchanging solutions about cells is efficient as well. The lateral migration velocity of cells in RInSE is slower than that of particles (Figure 6 b, red). This may be due to z-equilibrium positions closer to the channel centerline for cells. Cell

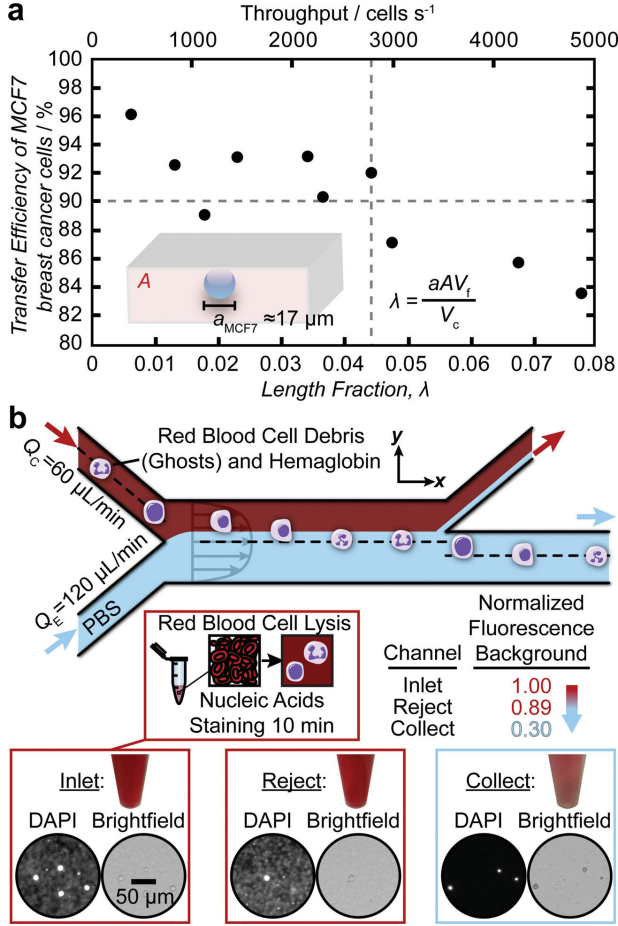


Figure 7. Demonstration of continuous cellular sample preparation. a) A plot of length fraction and throughput versus transfer efficiency for MCF7 breast cancer cells is shown. The inset shows the finite volume of a single equilibrium position. b) A schematic for utilization of RInSE to perform a typical preparation of stained leukocytes from a lysed whole blood sample using the microfluidic device is shown with cropped fluorescence (DAPI) and brightfield micrographs of the cellular sample before solution exchange and from the collection and rejection outlets of the device. RInSE removes RBC debris and reduces background fluorescence.

deformability has been demonstrated to shift inertial equilibrium positions towards the channel centerline, farther from the regions of the channel where wall effect lift acting in the y-direction is most dominant. The throughput (cells/s) of a single inertial solution exchange channel is limited by effects which detract from inertial focusing accuracy such as interparticle interactions and steric crowding of equilibrium positions which arise at high volume fractions of cells. Due to the finite volume of focusing regions, a length fraction, which takes these volumes into account, is a better descriptor than a volume fraction. We have previously defined the length fraction,  $\lambda$  ( $\lambda = aAV_f / V_c = 6 WHV_f / \pi a^2$ , where  $A$  is the cross-sectional area of the channel,  $V_f$  is the volume fraction of cells in suspension, and  $V_c$  is the mean volume of a single cell in the suspension). An intuitive understanding of the length fraction can be obtained by imagining a cylinder with a diameter matching that of the average cell diameter lying within the channel. Due to inertial focusing, cells will come to lie within this cylinder; however at higher concentrations, cells will fill the cylinder, prohibiting entry to other cells. The theoretical limit for highly accurate focusing is  $\lambda = 1$ , but practically, interparticle interactions lead to spacing between cells, and a lower  $\lambda$  should be employed for higher efficiency exchange. Further, at extremely high concentrations, cell-fluid disturbances are expected to act constructively, mixing the co-flow and resulting in lower purity of the exchange solution. We measured the transfer efficiency of harvested MCF7 cells into trypan blue with a range of  $\lambda$ . As expected, at lower  $\lambda$  ( $\lambda < 0.044$ , 2800 cells/s) efficiency remained high ( $\approx 90\%$ ), and at higher  $\lambda$  efficiency fell consistently below 90% (Figure 7).

In traditional cell-based assays, such as immunophenotyping or ploidy analysis by flow cytometry, cells are isolated from complex backgrounds (matrix) which confound the results of analytical measurements by centrifugation steps. Here, as a proof on concept we prepare stained leukocytes from whole blood via inertial solution exchange and without centrifugation steps to remove RBC debris (Figure 3 b). Whole blood was

diluted 10 $\times$  in a solution of red blood cell lysis buffer (ammonium chloride) containing a cell-permeable DNA dye (Hoechst 33324) off chip. After a 10 minute incubation, erythrocytes were lysed and leukocytes stained by the solution, but a large fluorescent background of hemoglobin and red blood cell ghosts was present without centrifugation. Instead of centrifugation, stained leukocytes were inertially transferred into a solution of PBS. As would be expected after a traditional wash, fluorescent micrographs of the inlet suspension and both outlet suspensions reveal a dramatic 70% reduction in background fluorescence by inertial solution exchange. As is evidenced by photographs of the collected fluid the transfer is not complete. Interactions between red blood cell

ghosts can be expected to result in contamination of the transfer solution, unlike operations with particles or cells from culture with a background that is largely molecular. However, brightfield images of the collected fluid show that this contamination is minimal and should be an effective background reduction for downstream STEAM analysis. Cells are not damaged by inertial flow conditions. Previous studies employing inertial lift forces for cell manipulation and sorting have demonstrated that the high flow velocity at which cells travel does not adversely affect their viability or alter their expression profile. While shear stresses experienced by cells are similar to those in experiments studying effects of fluid flow on cultured cells, the length of the exposure here is 4 to 5 orders of magnitude lower (10–20 ms versus minutes to hours). We postulate that transient exposure to shear is not sufficient to profoundly impact the cell.

We performed two proof-of-principle experiments to demonstrate how RInSE can be used for other applications in preparing breast cancer cells in blood for downstream imaging. We transferred MCF7s in a solution of methylene blue into a clean buffer at a throughput of approximately 1000 cells per second with 96% efficiency. We also transferred MCF7 cells coated with 1  $\mu$ m magnetic particles from a background of unbound particles into a clean buffer. In this experiment 91% of MCF7 cells were collected and 98% of free beads were removed.

### Hybrid Dispersion Laser Scanner

We have also developed a modification of the STEAM system that scans with a lower wavelength regime (800 nm) in a 1-D line scan mode that may lead to improved resolution image cytometry. Laser scanning technology is one of the most integral parts of today's scientific research, manufacturing, defense, and biomedicine. For sensing and imaging methods based on laser scanners, the ability to scan at high speeds is crucial for multi-dimensional evaluation of moving objects and dynamical processes. Here low scan rates result in motion blur and failure to capture fast transient information. Applications that require high scan rates (typically 1 kHz or higher in 2D) include identification of missiles and aircrafts via light detection and ranging (LIDAR), non-destructive inspection of acoustic instruments, structural dynamics, and microelectromechanical systems (MEMS) via laser-scanning surface vibrometry, and observation of biomechanical motility, cellular network dynamics, and neural activity via laser-scanning confocal and multi-photon microscopy. The central requirement for sensing and imaging of such events in real time is the temporal resolution shorter than the time scale of changes in the dynamical process. Furthermore, high-speed scanning capability is also important for high-throughput applications that require scanning a large area or many objects in a short period of time, such as geographical survey, atmospheric science, machine vision, laser TV systems, surface profilometry in the semiconductor industry, and endoscopy and cytometry for medical diagnosis.

Various types of laser scanning technology have been developed for higher scan rates in the past few decades. The most commonly used for beam steering are mechanically scanning mirrors known as galvanometric mirrors. Unfortunately, the galvanometric mirrors including MEMS scanners are slow due to inertia and provide linear scan rates only up to 10 kHz, resulting in aggregate 2D scan rates of 100 Hz at most. Another common type of laser

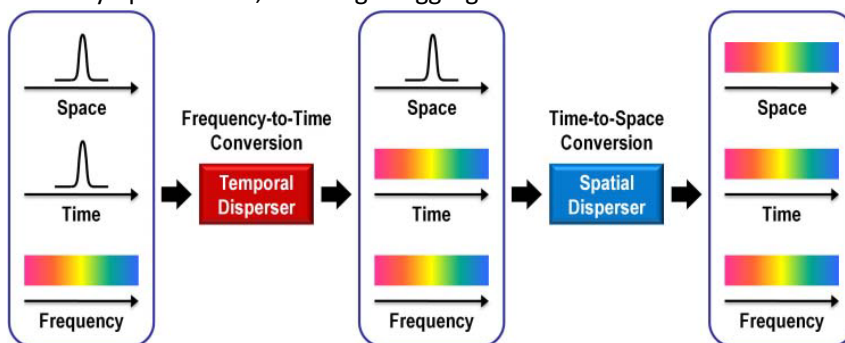


Figure 8. Concept of the HDLS. The operation of the HDLS consists of two steps: frequency-to-time conversion and time-to-space conversion. First, the broadband spectrum of an optical pulse is mapped into a temporal waveform by temporal dispersion. Second, the temporal waveform is converted into a 1D rainbow pulse in space by spatial dispersion. The resultant 1D rainbow pulse is incident onto an object, performing a 1D line scan. Combining the two steps, the spectrum of the pulse is mapped into space, resulting in each frequency component of the spectrum illuminating different spatial coordinates on the target at a different time. Pulses are repeated for repetitive scans at a rate equivalent to the pulse repetition rate.

scanners is acousto-optic deflectors (AODs) which provide 10 times higher scan rates than the traditional galvanometric mirrors by virtue of their acoustic frequency dependent diffraction (i.e., 100 kHz in 1D and 1 kHz in 2D). In addition, a combination of a frequency-tunable laser and diffractive optics has recently been found to operate as a laser scanner at scan rates comparable to AODs. To the best of our knowledge, these mechanisms provide the highest scan rates possible to date. We proposed and demonstrated a new method for laser scanning that enables

ultrafast inertia-free scans in the industrially and biomedically important spectral band (i.e., 800 nm) at 1000 times higher scan rates than conventional laser scanners. This approach is based on spatial dispersion of a broadband optical pulse onto the target with the pulse being linearly chirped by temporal dispersion so that each frequency component of the pulse arrives at a different set of spatial coordinates on the target at a different time. The scanner's ability to scan without the need for mechanical and active electronic components eliminates the speed bottleneck that exists in galvanometric mirrors and other techniques and hence enables ultrafast scanning at the rate equivalent to the laser's pulse repetition rate (typically 10–100 MHz). As a proof-of-principle demonstration, we show 1D line scans at more than 90 MHz and 2D raster scans at more than 100 kHz with 27,000 resolvable points and a dwell time of less than 60 ps. Furthermore, to show the broad utility of our method, we use it to demonstrate unique and previously difficult-to-achieve capabilities in imaging, surface vibrometry, and flow cytometry by virtue of its ultrahigh scan rates.

The concept of our laser scanner, which we refer to as the hybrid dispersion laser scanner (HDLS), is shown in Figure 8. Its operation consists of two steps: frequency-to-time conversion and time-to-space conversion. First, the broadband spectrum of an optical pulse is mapped into a temporal waveform by temporal dispersion. This step is known as wavelength-to-time mapping or dispersive Fourier transformation and is performed using large group-velocity dispersion (GVD) in dispersive fibers or chirped fiber Bragg gratings. Second, the temporal waveform is converted by spatial dispersion into a 1D rainbow pulse in space. The spatial disperser may be one or more prisms or diffraction gratings. The resultant 1D rainbow pulse is incident onto an object, performing a 1D line scan. Combining the two steps, the spectrum of the pulse is mapped into space, resulting in each frequency component of the spectrum

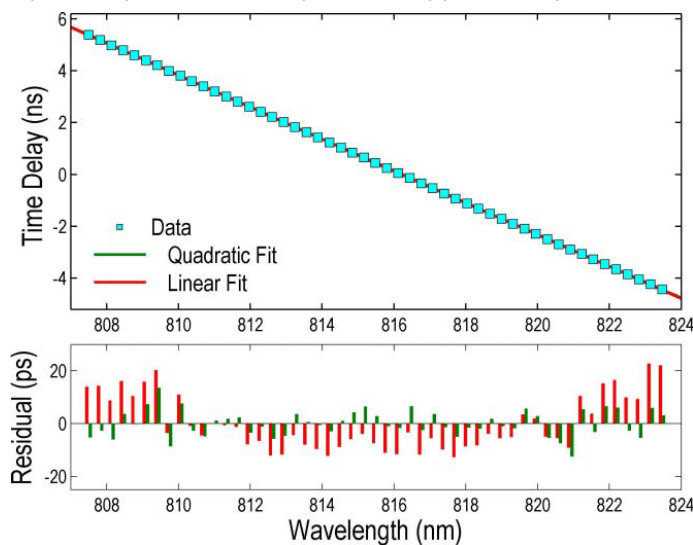


Figure 9. Chromatic dispersion of the dispersive fiber. To demonstrate dispersive Fourier transformation in the 800 nm spectral band, a single-mode fiber with a smaller effective mode area than conventional fibers in the wavelength operation range is employed. Consequently, the fiber provides increased contribution of waveguide dispersion to the total chromatic dispersion of the fiber (as large as 2123 ps/nm/km GVD), enabling dispersive Fourier transformation in this spectral range as indicated by the linear one-to-one relation between wavelength (frequency) and time as well as the small residuals between the data and fit functions.

wavelengths (See Methods). Also, the 800 nm spectral band is suitable for biomedical applications as it enables larger penetration depths in tissue and reduction in auto-fluorescence. To demonstrate dispersive Fourier transformation in this spectral band, we employ a single-mode fiber with a smaller effective mode field diameter (4  $\mu$ m) than conventional fibers in the wavelength operation range (typically 5–6  $\mu$ m). The fiber, hence, provides increased contribution of waveguide dispersion to the total chromatic dispersion of the fiber. Our chromatic dispersion

illuminating a different set of spatial coordinates on the target at a different time in series. The reflected, transmitted, or fluorescence light from the target can be detected by a single photodetector (e.g., a photodiode, photomultiplier tube, or avalanche photodetector). Pulses are repeated for repetitive scans at a rate equivalent to the pulse repetition rate. For 2D raster scans, a complementary scanner (i.e., the slow axis scanner) is used to scan the HDLS rainbow beam along the second planar dimension.

To maximize the practical utility of the HDLS, we design and implement it in the spectral range important for industrial and biomedical settings (i.e., 800 nm). For this purpose, we perform dispersive Fourier transformation in the 800 nm spectral band for the first time. Previously, dispersive Fourier transformation has been restricted to the fiber-optic communication band centered at 1550 nm due to the commercial unavailability of dispersive fibers with high dispersion-to-loss ratio outside the 1550 nm band. On the contrary, shorter wavelengths are desirable since the spectral resolution limited by diffractive elements (or equivalently the HDLS's number of resolvable points) improves with shorter

measurement indicates a large GVD of 2123 ps/nm/km (Figure 9), enabling dispersive Fourier transformation in this spectral band. This is a key improvement that will allow us to move STEAM imaging cytometry from 1550 nm band to the 800 nm band with expected improvements in cancer cell analysis performance.

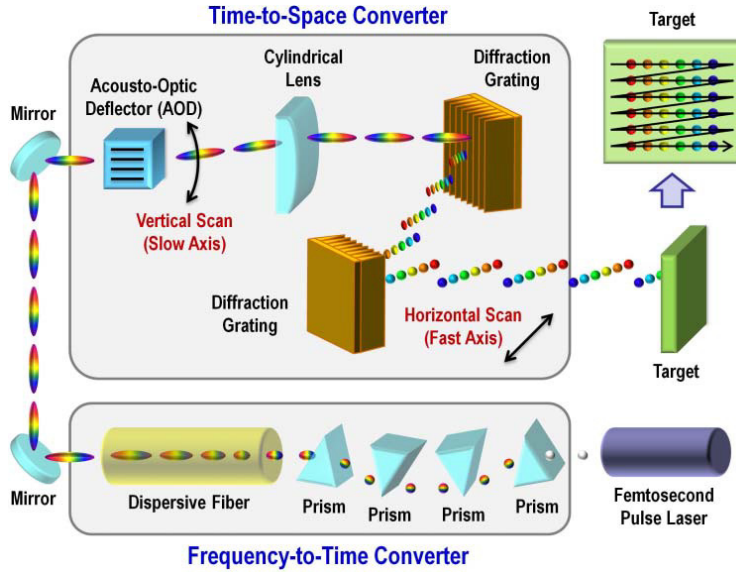


Figure 10. Schematic of the HDLS. The optical source is a Ti:Sapphire femtosecond pulse laser that generates a broadband pulse train at 90.8 MHz repetition rate. The pulses are pre-chirped by the prism-based pulse stretcher and enter the dispersive fiber in which the spectrum of each pulse is mapped into the time domain by the GVD of the fiber. A pair of diffraction gratings maps the pulses into space in the horizontal direction, producing 202 subpulses which arrive at different spatial coordinates on the target at different times. Consequently, 1D line scans are performed in the horizontal direction at 90.8 MHz. The AOD scans the pulses in the vertical direction at 105.4 kHz with 132 resolvable points, resulting in the aggregate resolution of 202 x 132 (horizontal x vertical) (See Methods). The cylindrical lens collimates the pulses deflected at different angles. The colors of the subpulses in the figure are only for illustrative purposes and do not represent the real wavelengths.

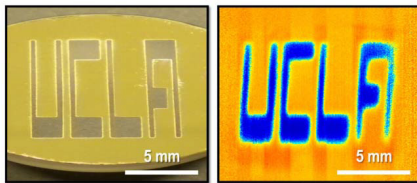
To demonstrate the HDLS, we constructed the apparatus shown in Figure 10. The optical source is a Ti:Sapphire femtosecond pulse laser that generates a train of broadband pulses at a pulse repetition rate of 90.8 MHz. Before entering the dispersive fiber, the pulses are prechirped by a prism-based pulse stretcher to avoid undesirable nonlinear interactions in the fiber. The pre-chirped pulses then enter the dispersive fiber in which the spectrum of each pulse is stretched into a temporal waveform due to the GVD of the fiber (2583 ps/nm). The AOD scans the pulses in the vertical direction with 132 resolvable points at a scan rate of 105.4 kHz (See Methods). A pair of diffraction gratings with 2200 lines/mm spatially disperses the pulses in the horizontal direction,

producing 202 resolvable subpulses (See Methods). When combined, the temporally dispersed pulses are scanned over the target by the gratings in the horizontal direction at 90.8 MHz (equivalent to the pulse repetition rate) and by the AOD in the vertical direction at 105.4 kHz for complete 2D raster scans.

To demonstrate the HDLS's one-to-one mapping between frequency, time, and space, we used it to conduct reflection imaging in real time. Figure 11a compares a CCD image of a test target and a

digitally reconstructed image of the target scanned by the HDLS. The HDLS image was reconstructed by mapping the reflection from the target measured by a photodetector into a 2D matrix using a separately measured pulse train and AOD driver signal. Figure 12b shows the performance of dispersive Fourier transformation in the 800 nm spectral range, validating one-to-one mapping between frequency (wavelength) and time and hence between time and space. The captured image clearly shows the word "UCLA," firmly establishing the HDLS based imaging.

(a)



(b)

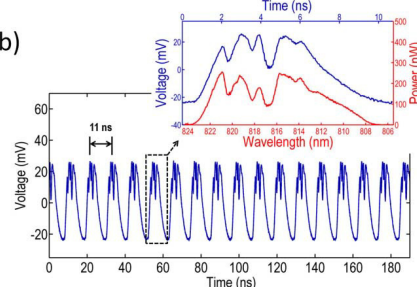
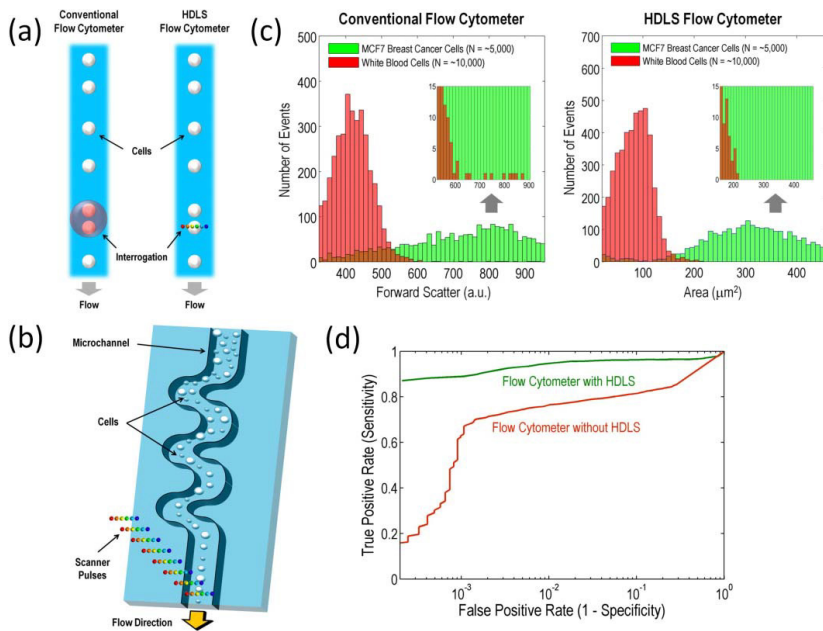


Figure 11. Imaging with the HDLS. (a) Comparison between a CCD image of the test target (left) and a digitally reconstructed image of the target scanned by the HDLS (right). The target consists of the non-reflective word "UCLA" on top of a reflective substrate and was scanned by the HDLS at 90.8 MHz in 1D and 105.4 kHz in 2D for image acquisition. The word "UCLA" appears evident (with the reddish and bluish colors indicating high and low reflectivities, respectively). The number of pixels in the target image is 510 x 861 (horizontal x vertical) (See Methods). The distortion on the right hand side of the letter "A" is due to the reduced diffraction efficiency of the AOD at a large deflection angle near the edge of the field of view. (b) Horizontal line scans (pulses) at different vertical coordinates (different deflection angles of the AOD) with a time interval of 11 ns, corresponding to the pulse repetition rate of 90.8 MHz. The inset shows one-to-one mapping between the reflection signal from the target measured by the photodetector and the spectrum of the signal measured by a conventional optical spectrum analyzer, clearly establishing the two-step transformation from time via frequency (wavelength) to space in the 800 nm spectral range. The wavelength dependence of the target's reflectivity is negligible as the bandwidth is less than 20 nm centered at 800 nm.



**Figure 12. Flow cytometry with the HDLS.** (a) Comparison in interrogation method between the conventional flow cytometer and HDLS-based flow cytometer. While conventional flow cytometers cannot resolve multiple cells (i.e., doublets, triplets, and clustered cells) within the interrogation beam due to the lack of spatial resolution, spatial metrics provided by the HDLS can be used to identify these events and hence reduce false positive rate and statistical error yet with high throughput. (b) Experimental apparatus for the HDLS-based flow cytometry. The microfluidic channel focuses and orders randomly distributed cells into a single stream with inertial lift forces (Supplementary Information). HDLS pulses are then focused onto the single stream of fast-flowing cells for forward-scattering measurements. Scattered light from the target is collected by an objective lens and detected by a single-pixel photodetector. To ensure stability, the microfluidic device was fabricated in thermoset polyester (TPE) using standard replica molding methods (Supplementary Information). The volumetric flow rate of cells was controlled by a syringe pump, and a uniform velocity of 1 m/s was achieved by positioning cells precisely in a velocity gradient using inertial focusing. (c) Comparison of size-based histograms obtained with the conventional flow cytometer (left) and the HDLS-based flow cytometer (right) using identical samples of white blood cells and MCF7 breast cancer cells (measured separately). The figure clearly indicates our method's ability to differentiate MCF7 breast cancer cells from white blood cells as it can identify multiple white blood cells as false positive events. (d) Receiver operating characteristic (ROC) curve analysis showing that flow cytometry with the HDLS achieves lower false positive rate than flow cytometry without it, yet with high sensitivity and high throughput (Supplementary Information). This is made possible by the complete spectrum in the spatial frequency domain provided by the HDLS's ultrafast laser-scanning capability.

Figure 12c compares size-based histograms of white blood cells and MCF7 breast cancer cells obtained by a conventional flow cytometer and the HDLS-based flow cytometer. It clearly indicates our method's ability to better differentiate MCF7 cells from white blood cells as it can identify multiple white blood cells as false positive events in traditional scatter measurements. Consequently, the false positive rate and statistical error of flow cytometry were reduced by virtue of the complete spectrum in the spatial frequency domain provided by the HDLS's ultrafast laser-scanning capability, yet with high sensitivity and high throughput (Figure 12d). Our method is expected to be a useful approach for high-precision size-based screening of rare breast cancer cells in complex biological samples.

We demonstrated the utility of the HDLS in rare cell screening of breast cancer cells defined in our statement of work. Flow cytometry is an indispensable tool for counting and analyzing a large heterogeneous population of cells in pathology, immunology, and genetics. Unfortunately, the false positive rate and statistical error of conventional flow cytometers are high due to the lack of spatial resolution, rendering the system theoretically less able to resolve multiple cells (i.e., doublets, triplets, and clustered cells) within the interrogation beam (Figure 12a). The ability to provide spatial metrics (i.e., spectra in the spatial frequency domain) with an ultrafast laser scanner can be used as a simpler and more accurate

method than other techniques to identify these events and hence reduce the false positive rate and statistical error. Specifically, the accuracy of the multiple-cell identification improves by a factor of the number of resolvable points or frequency bins in the spatial frequency domain (1,000) provided by the HDLS divided by two frequency bins (i.e., forward and side scattering) provided by conventional flow cytometers. Alternatively, high-speed laser scanners can also be used to perform high-throughput examination of many individual cells without the need for a single stream of cells. To demonstrate HDLS-based flow cytometry, we constructed the experimental setup shown in Figure 12b. Here we employed our inertial microfluidic technology to precisely position cells in flow with inertial lift forces while eliminating the need for sheath flow.

### **Key Research Accomplishments**

1. Construction of the optical system including the Nomarski prism in combination with STEAM optical imaging for high-speed, blur-free, and high-contrast image acquisition of MCF7 breast cancer cells
2. Validation of materials selection and selection of TPE as the optimal material for microfluidic device fabrication
3. Development of the real-time optoelectronic image processor and algorithms implemented on an FPGA that performs high-throughput image-based screening of a large number of cells and identification of rare cells
4. Demonstration of rapid inertial solutions exchange to remove red blood cell debris and excess particles that can be used inline to STEAM optical imaging
5. Development of a hybrid laser dispersion scanner using the 800 nm band that is expected to have higher speed and spatial resolution for identifying MCF7 cells from white blood cells.
6. Integration of the hardware and software into a combined system

### **Reportable Outcomes**

These key research accomplishments are supported by several reportable outcomes including five peer-reviewed journal publications over the last two years.

#### *Published manuscripts:*

A. M. Fard, A. Mahjoubfar, K. Goda, D. Gossett, D. Di Carlo, and B. Jalali, "Nomarski serial time-encoded amplified microscopy for high-speed contrast-enhanced imaging of transparent media," *Biomedical Optics Express*, vol. 2, no. 12, pp. 3387-3392, Nov. 2011.

E. Sollier, C. Murray, P. Maoddi, and D. Di Carlo, "Rapid prototyping polymers for microfluidic devices and high pressure injections," *Lab on a Chip*, vol. 12, no. 22, pp. 3752-3765, Oct. 2011.

D. Gossett, H. Tse, J. Dudani, K. Goda, T. Woods, S. Graves, D. Di Carlo, "Inertial manipulation and transfer of microparticles across laminar fluid streams," *Small*, vol. 8, no. 13, pp. 2757-2764, Jul. 2012.

K. Goda, A. Mahjoubfar, C. Wang, A. Fard, J. Adam, D. Gossett, A. Ayazi, E. Sollier, O. Malik, E. Chen, Y. Liu, R. Brown, N. Sarkhosh, D. Di Carlo, B. Jalali, "Hybrid dispersion laser scanner," *Scientific Reports*, vol. 2, no. 445, Jun. 2012.

K. Goda, A. Ayazi, D. Gossett, J. Sadasivam, C. Lonappan, E. Sollier, A. Fard, S. Hur, J. Adam, C. Murray, C. Wang, N. Brackbill, D. Di Carlo, B. Jalali. "High-throughput single-microparticle imaging flow analyzer," *Proceedings of the National Academy of Sciences of the USA*, vol. 109, no. 29, pp. 11630-5, Jul. 2012.

#### *Patents:*

Di Carlo D, Ozcan A, Jalali B, Tse HTK, Hur SC, inventors; Regents of the University of California, assignee. Sheathless Inertial Cell Ordering Microfluidic Device for Extreme Throughput Flow Cytometry. US Patent Application # (13/231,570). Filed 9/13/2011.

#### *Degrees / employment outcomes supported by this award:*

Daniel R. Gossett – Ph.D received in 2012, current position – Postdoctoral scholar at UCLA.

Soojung C. Hur – Ph.D. received in 2011, current position – Junior Fellow at the Rowland Institute at Harvard University.

Keisuke Goda, Ph.D. – obtained tenure track faculty position at University of Tokyo.

Elodie Sollier, Ph.D. – obtained current position as Vice President of R&D at Vortex Diagnostics.

#### *Funding applied for:*

Pending, NIH R01 for circulating tumor cell detection from blood in breast cancer patients.

#### **Conclusion**

In summary, we have developed a high-throughput single-cell flow-through image analyzer for real-time image acquisition and screening of rare breast cancer cells from blood with high sensitivity, high statistical accuracy and high contrast. We estimate that newly demonstrated 800 nm band laser scanner imaging and higher contrast nomarski imaging can improve these results further. Further, inline sample preparation of cellular samples with inertial microfluidics can reduce false positive rates by excluding cell debris. In the future, our method can also be combined with a conventional cell sorter to sort out rare breast cancer cells for further companion diagnostics e.g. for HER2 mutants that could respond to Herceptin.

#### **References**

- [1] K. Goda, K. K. Tsia, and B. Jalali, "Serial time-encoded amplified imaging for real-time observation of fast dynamic phenomena," *Nature*, vol. 458, no. 7242, pp. 1145-1149, Apr. 2009.
- [2] A. M. Fard, A. Mahjoubfar, K. Goda, D. Gossett, D. Di Carlo, and B. Jalali, "Nomarski serial time-encoded amplified microscopy for high-speed contrast-enhanced imaging of transparent media," *Biomedical Optics Express*, vol. 2, no. 12, pp. 3387-3392, Nov. 2011.
- [3] E. Sollier, C. Murray, P. Maoddi, and D. Di Carlo, "Rapid prototyping polymers for microfluidic devices and high pressure injections," *Lab on a Chip*, vol. 12, no. 22, pp. 3752-3765, Oct. 2011.
- [4] D. Di Carlo, D. Irimia, R. G. Tompkins, and M. Toner, "Continuous inertial focusing, ordering, and separation of particles in microchannels," *Proceedings of the National Academy of Sciences of the United States of America*, vol. 104, no. 48, pp. 18892-18897, Nov. 2007.
- [5] D. R. Gossett and D. Di Carlo, "Particle focusing mechanisms in curving confined flows," *Analytical Chemistry*, vol. 81, no. 20, pp. 8459-8465, Oct. 2009.
- [6] D. Gossett, H. Tse, J. Dudani, K. Goda, T. Woods, S. Graves, D. Di Carlo, "Inertial manipulation and transfer of microparticles across laminar fluid streams," *Small*, vol. 8, no. 13, pp. 2757-2764, Jul. 2012.
- [7] K. Goda, A. Mahjoubfar, C. Wang, A. Fard, J. Adam, D. Gossett, A. Ayazi, E. Sollier, O. Malik, E. Chen, Y. Liu, R. Brown, N. Sarkhosh, D. Di Carlo, B. Jalali, "Hybrid dispersion laser scanner," *Scientific Reports*, vol. 2, no. 445, Jun. 2012.

#### **Appendices**

##### **N-STEAM**

The N-STEAM's enhanced image-contrast can be obtained as follows. It can be adjusted using the offset phase shift between the two spatially-dispersed orthogonally-polarized beams. Similar to the expression derived in Ref. [22]. for conventional DIC or Nomarski microscopy, the intensity of each wavelength component of the interfered beam in N-STEAM is obtained by the expression,

$$[ \quad +$$

where  $\gamma = \cos 2(\varphi_A - \varphi_P)$  and  $\beta = -0.5 \sin(2\varphi_A) \sin(2\varphi_P)$ . Here  $\varphi_A$  and  $\varphi_P$  are the angles of the analyzer and polarizer, respectively, and  $\delta$  is the differential phase shift between the two polarized beams. In N-STEAM, the polarizer and analyzer are the same as illustrated in Fig. 1(a); hence,  $\varphi_A$  and  $\varphi_P$  are equal to 45 degrees. The differential phase shift ( $\delta$ ) is composed of two parts: the phase shift offset and the phase shift due to the optical path length difference between the incident points on the object to be imaged. The phase shift offset is a constant phase shift due to different optical paths travelled by the two spatially-dispersed beams. This can be adjusted by changing the tilt angle of the prism with respect to the propagation direction of the illumination beam.

The specification of N-STEAM demonstrated here is evaluated as follows. The number of image pixels is found to be

$$N = |D| \cdot \Delta\lambda \cdot f_{\text{dig}} = 1373$$

where  $D$  is the total dispersion in the dispersive fiber ( $D = 1373$  ps/nm),  $\Delta\lambda$  is the optical bandwidth ( $\Delta\lambda = 20$  nm), and  $f_{\text{dig}}$  is the sampling rate of the digitizer ( $f_{\text{dig}} = 50$  GS/s). The diffraction-limited spatial resolution is

$$d \approx \lambda/2/NA \approx 2 \mu\text{m}$$

where  $\lambda$  is the operation wavelength ( $\lambda = 1591$  nm) and  $NA$  is the numerical aperture of the objective lens ( $NA = 0.4$ ). The number of resolvable spectral points is estimated to be  $\sim 180$  from the spectral resolution of the ADFT process [23]. Hence, the dwell time (shutter speed) is found to be  $\sim 33$  ps from the bandwidth of each subpulse or wavelength component ( $20$  nm /  $180$ ) in the line scan. The current implementation of the N-STEAM provides a 1D line-scan width of  $100 \mu\text{m}$ ; this has been validated using a known target (Resolution test target, Thorlabs, R2L2S1N).

#### RInSE

*Numerical Calculation of Inertial Lift Forces:* Inertial lift force was calculated using COMSOL Multiphysics (Comsol, Inc., Burlington, MA, USA) as previously described. The numerical solution is for a  $10 \mu\text{m}$  sphere in a high aspect ratio channel ( $80$  by  $40 \mu\text{m}$ ) with a mean flow velocity of  $1$  m/s. The fluid properties, viscosity and density, are that of water.

*Measuring Size Dependence of Lateral Migration:* Polydisperse polydimethylsiloxane (PDMS; Sylgard 184 Silicone Elastomer Kit; Dow Corning Corp., Midland, MI, USA) particles were synthesized as previously described. A  $40 \mu\text{m}$  pore size cell strainer was used to remove large particles. The particle suspension was pumped into the particle and cell inlet at  $70 \mu\text{L/min}$ , while sterile filtered trypan blue (Thermo Fisher Scientific Inc., Waltham, MA, USA) was pumped into the exchange solution inlet at  $120 \mu\text{L/min}$  using PHD 2000 syringe pumps (Harvard Apparatus, Holliston, MA, USA). The lateral migration velocity was measured from high-speed video using a custom particle tracking algorithm written in MATLAB (MathWorks, Natick, MA, USA). Video was acquired at  $555$  frames per second ( $18 \mu\text{s}$  interval) with a  $1 \mu\text{s}$  shutter speed using a Phantom v7.3 high speed camera at  $800 \times 56$  pixels mounted on a Nikon Ti Inverted Microscope and a  $10\times$  objective lens (resulting in  $2.22 \mu\text{m}$  per pixel). The lateral migration velocity was defined as distance traveled perpendicular to primary flow in  $325$  pixels divided by the time required to travel this distance. This method was chosen because automated measures of smaller lateral position were not accurate enough to achieve meaningful velocities and within  $325$  pixels most particles were still migrating laterally. Particle migration velocity was measured by a MATLAB script while cell migration was measured by hand. Change in grayscale intensity of polystyrene particles was quantified by ImageJ (U.S. National Institutes of Health, Bethesda, Maryland, USA, <http://imagej.nih.gov/ij/>).

*Measuring Solution Exchange Efficiency and Purity:*  $19 \mu\text{m}$  polystyrene particles (CV  $\leq 16\%$ ; Thermo Fisher Scientific Inc., Waltham, MA, USA) were diluted in deionized water and transferred into a solution of sterile-filtered trypan blue. High-speed microscopic images were recorded at the channel outlet. The transfer efficiency of the  $19 \mu\text{m}$  polystyrene particles was calculated from hemacytometer counts of the initial suspension and the outlets. The purity of the transfer fluid in the collection outlet, defined as the ratio of absorbance in the collection outlet to that of the inlet, was quantified by an Infinite 200 Microplate Reader (Tecan Group Ltd., Männedorf, Switzerland). The cellular

preparation efficiency was calculated using multiple concentrations of the MCF7 cell line (breast epithelial; culturing and harvesting details below). MCF7 cells were transferred into a solution of sterile-filtered trypan blue and visual observation of high-speed microscopic images yielded efficiency,  $(100 \cdot \text{Collected Cells} / \text{Total Cells Observed})$ .

*Cell Samples and Experiments:* Whole blood was drawn from consenting donors with approval from the UCLA Institutional Review Board. Hoechst 33342, trihydrochloride, trihydrate— 10 mg/mL solution in water (Invitrogen Corp., Carlsbad, CA, USA)—was diluted to 1  $\mu\text{g/mL}$  in red blood cell lysis buffer (ammonium chloride; Roche Diagnostics Corporation, Indianapolis, IN, USA). A smaller embodiment of the microchannel was used to work with blood cells (channel widths scaled to 75%). The MCF7 cell line was cultured in Dulbecco's Modified Eagle Medium (DMEM) with L-glutamine, 4.5g/L glucose and sodium pyruvate (Mediatech, Inc., Manassas, VA, USA) with 10% fetal bovine serum (Thermo Fisher Scientific Inc., Waltham, MA, USA) and 1% Penicillin-Streptomycin (Invitrogen Corp., Carlsbad, CA, USA). MCF7 cells were harvested with 0.25% porcine trypsin (Thermo Fisher Scientific Inc., Waltham, MA, USA). In cases where live cells were used, the cells were resuspended in Dulbecco's Phosphate Buffered Saline (PBS; Thermo Fisher Scientific Inc., Waltham, MA, USA). When fixed cells were used, the cells were resuspended in 4% formaldehyde for 10 minutes before being resuspended in PBS.

*Imaging Methylene Blue-Stained Cells:* Cells stained with methylene blue and with a background of methylene blue were imaged with a color Go-3 CMOS Camera, employing QCapture software (QImaging, Surrey, BC, Canada) to control exposure time. Identical camera settings were used when imaging stains before and after processing by RInSE.

*Coating Cells with 1  $\mu\text{m}$  Magnetic Particles:* Fixed MCF7 cells, cultured, harvested, and fixed as described above, were incubated for 30 minutes in biotinylated anti-human CD326 (EpCAM) (EBioscience, Inc., San Diego, CA, USA). Cells were washed twice with PBS then resuspended in PBS with 1  $\mu\text{m}$  streptavidin-coupled dynabeads (Invitrogen Corp., Carlsbad, CA, USA) and placed on an incubated shaker until used. Flow conditions in rotation experiments with coated cells were similar to those for uncoated MCF7 cells.

*Fluorescence Detection:* The fluorescence detection setup is depicted in Figure S4 of the SI. A continuous-wave laser (Laser Quantum, San Jose, CA, USA) operating at 532 nm was focused into a fiber assembly (LEONI Fiber Optics, Inc., Lightfoot, VA, USA) by a fiber coupler to deliver 10 mW onto cells in flow. The end of the assembly connected to this lens was a close-packed bundle of twelve 100  $\mu\text{m}$  multimode fibers. Half way (50 cm) along the fiber bundle it was wrapped around a single 400  $\mu\text{m}$  multimode fiber. A fused silica focusing and imaging beam probe (Oriel Instruments, Newport Corp., Irvine, CA, USA) was connected to the fiber assembly by its SMA connection at the end with all 13 fibers. The beam probe, containing two lenses, had a working distance of 12 mm and a magnification of 1x and was focused onto the microchannel. Light was collected back through the fiber probe and the 400  $\mu\text{m}$  core multimode fiber. The other end of the core fiber was connected to a 30 mm lens cube by its SMA connection. A dichroic beamsplitter directed emitted light through a band-pass filter, with a center wavelength of 575 nm and full width half maximum of 40 nm (Chroma Technology Corp., Bellows Falls, VT, USA), into a photomultiplier tube (H10723-01; Hamamatsu City, Shizuoka Pref., Japan). The signal was digitized by a digitizer (National Instruments, Austin, TX, USA) at a sampling rate of 1 MS/s. Lowpass filtering was performed on the digitized signal in MATLAB (The MathWorks, Inc., Natick, MA, USA) to remove high-frequency noise on the fluorescence signal. 10  $\mu\text{m}$  Envy Green (excitation: 525 nm, emission: 565 nm) microspheres (Bangs Laboratories, Inc., Fishers, IN, USA) were suspended in a solution of phycoerythrin and inertially transferred into a solution of phycoerythrin of the same concentration to mimic the before solution exchange state. Beads in the same initial suspension were also inertially transferred into water to mimic the after solution exchange state. The fiber probe was situated above the same location of the 'collect' outlet for both measurements. Peak height, noise floor and standard deviation were extracted in MATLAB in order to calculate the signal-to-noise ratio. The signal-to-noise ( $\text{SNR} = (h - n) / s$ ), where  $h$  is the average of absolute peak heights,  $n$  is the mean noise level, and  $s$  is the standard deviation of the noise. Here, we sought to simulate conditions with a dim signal, where cell or particle peaks could easily be confused with the noise but on average large enough to quantify; thus, we used beads with fairly uniform intensities instead of labeled cells. For this experiment we made small modifications to the microchannel; specifically, we lengthened the particle collection outlet to accommodate

the spatial needs of the fiber probe and the outlet tubing. We also created a second particle inlet to allow greater concentrations of particles and improved downstream focusing. For an accurate comparison of pre- and post-solution exchange conditions we maintained a fixed position for the focal spot; therefore, particle velocity and other factors affecting signal and noise levels would be constant.

*Statistics:* To determine the scaling of particle diameter with lift force, particle diameter and lift force were log transformed and linearly fit in MATLAB using the 'fit' function. The function returned the scaling and a goodness-of-fit coefficient of determination,  $R^2$ . Standard deviations were also calculated in MATLAB. Linear regression was performed to determine if there was a correlation between cell diameter and cell velocity.

## Hybrid Dispersion Laser Scanner

### Designer's equations for the HDLS

We discuss the “designer's equations” which predict the performance of the HDLS. Here the key parameters are the number of resolvable points, dwell time, and scan rate. Since these parameters are not independent, but interrelated, values for them need to be chosen carefully in order to optimize the performance of the scanner. First, the number of resolvable points ( $n_{\text{HDLS}}$ ) is determined by the total optical bandwidth ( $\Delta\lambda$ ) and the spectral resolution limited by the temporal dispersion or the temporal analog of the far-field spectral resolution<sup>26</sup> ( $\delta\lambda_t$ ) as well as the spectral resolution limited by the spatial dispersion<sup>37, 38</sup> ( $\delta\lambda_s$ ). It is given by

$$n_{\text{HDLS}} = \Delta\lambda / \max(\delta\lambda_t, \delta\lambda_s) \quad (1)$$

where  $\delta\lambda_t$  and  $\delta\lambda_s$  are given by

$$\delta\lambda_t = \lambda_0 \sqrt{2/c|D|} \quad \text{and} \quad \delta\lambda_s = \lambda_0 \cos \theta / Gd, \quad (2)$$

respectively. Here we have assumed that the temporal and spatial dispersers are a dispersive fiber and diffraction grating, respectively.  $c$  is the speed of light in vacuum,  $\lambda_0$  is the center wavelength of the broadband pulse laser in vacuum,  $D$  is the temporal dispersion or GVD,  $\theta$  is the Littrow blaze angle of the incident beam with respect to the grating,  $G$  is the groove density of the grating, and  $d$  is the diameter of the beam incident on the grating. It is desirable to match the values of the two spectral resolutions to avoid any unnecessary dispersion. In our demonstration, they have comparable values based on the measured center wavelength ( $\lambda_0 = 814$  nm), optical bandwidth ( $\Delta\lambda = 17.5$  nm), GVD ( $D = -583$  ps/nm), groove density ( $G = 2200$  lines/mm), beam diameter ( $d = 3$  mm), and Littrow blaze angle ( $\theta = 60^\circ$ ), resulting in 202 resolvable points. Second, the time during which the HDLS dwells on each resolvable point or the so-called dwell time ( $\tau_{\text{HDLS}}$ ) is found to be

$$\tau_{\text{HDLS}} = D \max(\delta\lambda_t, \delta\lambda_s). \quad (3)$$

In our demonstration, the dwell time is found to be 51 ps. Finally, the scan rate is equivalent to the pulse repetition rate of the broadband pulse laser. However, there is an upper limit on the scan rate ( $R_{\text{HDLS}}$ ) to avoid overlaps of consecutive temporally-dispersed pulses. The limit is given by

$$R_{\text{HDLS}} < R_{\text{max}} = (D\Delta\lambda)^{-1}. \quad (4)$$

In our demonstration, the limit on the scan rate is found to be  $R_{\text{max}} = 98$  MHz, which is higher than our scan rate (90.8 MHz) and hence satisfies the requirement. All these equations are important for designing the HDLS and optimizing its performance.

### Performance of the AOD

The number of resolvable points along the AOD's scan direction is given by  $n_{\text{AOD}} = \alpha B(1 - \alpha/vT)/\xi v$ , where  $\alpha$  is the AOD's aperture,  $B$  is the acousto-optic bandwidth,  $v$  is the acoustic velocity,  $T$  is the total frequency modulation scan time, and  $\xi$  is the characteristic beam shape parameter<sup>19</sup>. In our proof-of-principle demonstration ( $2/T = 105.4$  kHz), the number is found to be  $n_{\text{AOD}} = 132$  from  $\alpha = 6$  mm,  $B = 100$  MHz,  $v = 4.2$  km/s, and  $\xi = 1$ .

### Dispersion measurement

To measure the GVD of our dispersive fiber, we employed the method reported by Hult *et al*<sup>39</sup> which is based on a time-of-flight technique combined with a supercontinuum light source. It enables measurement of GVD with high

spectral resolution over a large spectral range. The linear and quadratic fit functions were found to be  $y = -(0.615 \text{ ns/nm})x + (502 \text{ ns})$  and  $y = (0.000514 \text{ ns/nm}^2)x^2 - (1.45 \text{ ns/nm})x + (843 \text{ ns})$ , respectively, where  $x$  is the wavelength in units of nm.

#### Reflection imaging with the HDLS

We derive the number of pixels in the target image. In the experiment, the back-reflected light from the target is detected via an optical circulator by a high-speed photodetector with 12 GHz bandwidth. The output of the photodetector is digitized by a real-time digitizer with 16 GHz bandwidth and 50 GS/s sampling rate. The number of pixels in the target image is found from the GVD ( $D = -583 \text{ ps/nm}$ ), the sampling rate of the digitizer ( $f_{\text{dig}} = 50 \text{ GS/s}$ ), the optical bandwidth ( $\Delta\lambda = 17.5 \text{ nm}$ ), the pulse repetition rate ( $R = 90.8 \text{ MHz}$ ), and AOD scan rate ( $r = 2/T = 105.4 \text{ kHz}$ ) to be

$$N_{\text{HDLS}} \times N_{\text{AOD}} = (D \times f_{\text{dig}} \times \Delta\lambda) \times (R/r) = 510 \times 861 \text{ pixels}, \quad (5)$$

where  $x$  and  $y$  are the transverse axes orthogonal to the propagation axis of the incident light.

#### Surface vibrometry with the HDLS

We discuss the method for generating axially resolved surface profiles. To precisely measure the surface profile of the vibrating target, we employ Michelson interferometry in which the vibrating target and a fixed reference mirror are placed at the end of the interferometer's sample and reference arms, respectively. Here the axial position of each scanned point on the surface is encoded into the output intensity of the interferometer (i.e., the interferogram in the time domain), which is given in the form of

$$I(x, y, z) = I_0(x, y) + I_1(x, y) \cos[\phi_0 + \phi_1(x, y, z)]. \quad (6)$$

where  $I_0(x, y)$  is the intensity profile of the incident light on the target,  $I_1(x, y)$  is the intensity profile of the reflected light from the target,  $\phi_0$  is the initial phase difference between the two arms of the interferometer, and  $\phi_1(x, y, z)$  is the phase profile of the target. Here  $x$  and  $y$  are the axes in the transverse plane while  $z$  is the axis along the axial direction. By introducing a relatively large phase shift between the two arms, the second term can vary much more rapidly than the first term. Then, high-pass filtering Eq. (6) removes the first term, yielding

$$I_{\text{HP}}(x, y, z) = I_1(x, y) \cos[\phi_0 + \phi_1(x, y, z)]. \quad (7)$$

Applying Hilbert transformation<sup>22</sup> to the high-pass filtered interferogram generates

$$H[I_{\text{HP}}(x, y, z)] = I_1(x, y) \sin[\phi_0 + \phi_1(x, y, z)]. \quad (8)$$

Hence, the phase profile of the surface can be retrieved from Eqs. (7) and (8),

$$\phi_1(x, y, z) = \tan^{-1} \{H[I_{\text{HP}}(x, y, z)]/I_{\text{HP}}(x, y, z)\} - \phi_0, \quad (9)$$

and hence the axial displacement profile of the surface is given by

$$d(x, y) = \phi_1(x, y, z)/k(x, y) = \lambda(x, y)\phi_1(x, y, z)/2\pi \quad (10)$$

where  $k(x, y)$  and  $\lambda(x, y)$  are the wavenumber and wavelength of the incident light, respectively, and depend on the spatial coordinates of the interrogation point. In our proof-of-principle experiment, the axial resolution ( $\delta z$ ) is found to be 0.4 nm from the expression,  $\delta z = 2^{-b}/k \sin 2k(z_0 + z)$ , where  $z_0$  is the initial offset to the sample arm length with respect to the reference arm length ( $\phi_0 = kz_0$ ) and  $b$  is the digitizer's improved effective number of bits (ENOB) ( $b = 8.3$  bits). The number of pixels in the image of the vibrating target is the same as in the reflection imaging experiment ( $510 \times 861$  pixels).

#### Conventional flow cytometry

MCF7 breast cancer epithelial cells were harvested from culture and fixed by a 10-minute incubation in 4% formaldehyde. Cells were washed and resuspended in PBS. Whole blood, obtained with an approved Institutional Review Boards protocol, was mixed with red blood cell lysis buffer (Roche) at a ratio of 2 (lysis buffer) to 1 (whole blood) and incubated for 10 minutes. White blood cells were washed once in lysis buffer then resuspended in PBS. MCF7 and white blood cell suspensions were analyzed with the FACSCalibur system in the Flow Cytometry Core Laboratory at UCLA.

#### Flow cytometry with the HDLS

The microfluidic device was fabricated in thermoset polyester (TPE). We used samples of white blood cells and MCF7 breast cancer cells identical to those used for analysis with the FACSCalibur system. The volumetric flow rate of cells was controlled by a syringe pump, and a uniform velocity of 1 m/s was achieved by positioning cells precisely in a

velocity gradient using inertial focusing. HDLS pulses are focused onto the cells in the microchannel via an objective lens with a numerical aperture of 0.4. The 2D spatial metrics of cells were obtained by the combination of forward scattered light from 1D HDLS scans and the flow. The scattered light was collected via the same objective lens by the high-speed photodetector with 12 GHz bandwidth, and the output signal was digitized by the real-time digitizer with 16 GHz bandwidth and 50 GS/s sampling rate (identical to the detector and digitizer used in the experiment for Figure 11).